In-Situ γ-γ' Lattice Parameter Evolution and Tertiary Burst Phenomena During Controlled Cooling of Commercial PM Nickel-Base Superalloys

NICHOLAS J. KRUTZ, YAN GAO, YANG REN, IAN SPINELLI, and MICHAEL J. MILLS

The γ and γ' lattice parameter evolution of two commercial powder metallurgy (PM) nickel-base superalloys, ME3 and Rene'88DT, during cooling from above the γ' prime solvus temperature is characterized using in-situ synchrotron X-ray Diffraction (XRD). The peak intensity deconvolution necessary for quantifying misfit between the two phases from XRD is accomplished by combining direct observation of several superlattice peak positions with thermodynamic modeling to quantify the intensity relationship between the overlapping phases. The misfit values obtained from the XRD measurements are compared to Scanning Electron Microscopy (SEM) observations of γ' precipitate shapes for a subset of the experimental conditions where it can be observed that the exposures that result in cuboidal precipitate shapes are associated with the highest degrees of relative misfit. Time-resolved observations of the on-cooling lattice parameter evolution suggest a potential direct observation of the tertiary γ' burst events in the two compositions within both the (100) superlattice peak and the (311) fundamental peak. The onset temperatures for the tertiary γ' burst events for ME3 and Rene'88DT compositions for the cooling rates examined were found to be approximately 925 °C and 815 °C, respectively.

I. INTRODUCTION

POWDER metallurgy (PM) nickel-base superalloys play a critical role in modern-day gas turbine disk design. This is owed largely to their inherent process homogeneity which results in repeatable microstructural features and mechanical properties making them vitally important for high-pressure gas turbine components for aerospace. The ability for these alloys to sustain strength at temperature is due to the precipitation of a coherent, ordered phase known as γ' that serves as the primary intragranular strengthening mechanism. The real-time evolution of these precipitates during processing remains a highly significant area of study in terms of alloy process design and optimization.

A common heat treatment applied to some nickel-base superalloys includes a supersolvus solutioning step which yields a multimodal distribution of γ' precipitates upon cooling.[1] Supersolvus solutioning results in the full dissolution of primary γ' particles that are formed during upstream processing, producing a coarsened grain structure. The precipitates that form on-cooling from solutioning have been shown to be strongly influenced by cooling rates, both in composition[2–4] and morphology.[5–7] Some commercial alloys that have been produced with supersolvus solutioning heat treatments include Rene'95,[8] Rene'88DT,[9] ME3,[10] and IN100.[11] Other common heat treatments of advanced superalloys include a dual heat treatment approach, where the bore of the turbine disk receives a subsolvus thermal exposure and the rim receives a supersolvus thermal exposure that achieves a locally optimum set of properties for the component.[12] While commercially produced alloys typically undergo subsequent isothermal aging steps to refine the γ' structure, this study aims at focusing on the transient period directly after supersolvus solutioning.

The formation of γ' and the overall complexity of the γ' morphology—size, shape, interparticle spacing, and number density—have been shown to be crucial in creep performance of γ' strengthened nickel-base superalloys.[13] During precipitation, the transformation from

NICHOLAS J. KRUTZ is with the GE Aviation, One Neumann Way, Cincinnati, OH 45215 and also with the Department of Materials Science and Engineering, The Ohio State University, 2041 College Rd, Columbus, OH 43210. Contact e-mail: nicholas.krutz@ge.com YAN GAO and IAN SPINELLI are with the GE Research, 1 Research Circle, Niskayuna, NY 12309. YANG REN is with the Argonne National Laboratory, Advanced Photon Source, 9700 South Cass Avenue, Lemont, IL 60439. MICHAEL J. MILLS is with the Department of Materials Science and Engineering, The Ohio State University.

γ to γ′ results in a volumetric change of the transformed material. The quantity used to describe this difference in lattice parameter is referred to as lattice misfit and has been shown to have a strong compositional dependence[14] and varies with temperature coinciding with thermal expansion and contraction of the crystal lattices.[15] The study and optimization of the lattice misfit has been researched extensively in the context of single-crystal superalloy materials used for turbine blade applications.[15–17] The magnitude of the misfit has also been shown to strongly influence grain boundary morphology and creep rupture properties of the material.[18]

The γ′ precipitation mechanism itself has been a widely studied topic area with special attention towards the mechanistic changes that govern the different generations of γ′ nucleation events or bursts. Following classical nucleation theory, as the material is cooled below the γ′ solvus temperature, the balance of driving force, interfacial energy, and diffusivity invokes the initial burst of γ′ which, by convention, is referred to as secondary γ′.[19] As the temperature continues to decrease, the diffusivity slows and the growth of existing γ′ nuclei is inhibited. Eventually, the degree of matrix supersaturation exceeds a critical level for the nucleation driving force of an additional population of γ′ precipitate, referred to as tertiary γ′.[20]

Traditionally, the role of misfit on γ′ precipitation depends on the stage of evolution—that is, nucleation, growth, or coarsening—of the system being evaluated. Often in first-order approximations of γ′ nucleation, it is assumed that there is minimal contribution from volumetric strain energy in determining the nucleation driving force for secondary γ′ precipitates.[19,21] As a γ′ nucleus grows, interfacial diffusion along with elastic anisotropy of the cubic crystal structure in the presence of misfit results in precipitate growth in the preferred crystallographic orientations, yielding cuboidal, octet, or even faceted dendrite γ′ particles.[22,23] In the context of fully coherent, fully grown precipitates, the free energy of the precipitates has contributions from both the interfacial energy and coherency strain energy due to misfit which contribute to the equilibrium precipitate shape. During subsequent thermal exposure, the continued evolution of the precipitates can lead to a loss of coherency with increasing size. The size at which this occurs aligns with when the free energy penalty associated with a higher interfacial energy is less than the coherency strain energy.[24] In this context, evaluating misfit as a function of time and temperature for different disk alloys can serve to enhance our understanding of alloy stability during subsequent age heat treatments and service conditions.

The characterization of γ and γ′ lattice parameter evolution and its role in processing of nickel-base superalloys in terms of temperature dependence have been generally considered for a wide range of alloy compositions. Nathal, et al., acquired lattice parameter data on fully formed, semi-coherent γ′ precipitates on Ni-0.6Mo-0.92Ta-12.5Al-1.83Ti-10.5Cr-3.3W single crystals at elevated temperatures using a lab X-Ray source.[15] Several in-situ diffraction measurements for quantifying misfit have been performed on the IN718 composition including neutron diffraction[25,26] owing to the significance of γ-γ″, as opposed to γ-γ′, misfit on the formation of the γ″ precipitates and the role of misfit within the deformation response of the alloy. Studies performed on model superalloy compositions by Goodfellow, et al., using neutron diffraction[14] and Collins, et al, synchrotron X-ray diffraction[27] show that typical γ-γ′ misfit for these alloys is generally less than 0.5 pct for the range of W and Ta contents and temperatures evaluated. In-situ synchrotron X-Ray characterization of the Rene'88DT γ′ burst response was performed by Singh, et al.,[2] however, no information pertaining to misfit or the evolution of the γ lattice parameter as a function of temperature was reported. Similarly, in-situ synchrotron X-ray characterization of PM nickel-base superalloy LSHR was performed,[19] yet only a limited amount of information pertaining to time–temperature dependence of the superlattice peaks was reported. It is within this context that we further quantify the effect of misfit within the commercial PM nickel-base superalloy composition space. Further need for characterization in this domain is being driven by new design considerations as increasingly capable alloys are required for next-generation gas turbine designs.[28]

Within this study, we further the understanding of PM superalloy process metallurgy by using in-situ X-Ray characterization, which has only been partially conveyed in this subset of the literature to date. To develop this understanding, this work is divided into two segments. In the first, the instantaneous on-cooling γ′ evolution of two PM nickel-base superalloys is interrogated and compared to one another. The conditions employed are representative of processing steps similar to those experienced during industrial processing. Successful interpretation of misfit between the matrix and precipitate phases relies on a careful peak-deconvolution methodology that is also presented. In the second portion of the study, the time dependence of the γ′ evolution as it cools from a supersolvus state on a single PM alloy is investigated using in-situ subsolvus isothermal hold experiments and compared to the instantaneous γ′ response. From this, generalized conclusions are made regarding the ability to manipulate misfit using cooling rate and the observed time–temperature effects.

II. EXPERIMENTAL PROCEDURE

A. *Materials and Processing*

The input material for this study was obtained from full-scale forgings of two PM nickel-base superalloys: ME3 and Rene'88DT that were provided by GE Aviation (Evendale, Ohio) and had received a subsolvus isothermal forge prior to receipt. A Backscattered Electron (BSE) image of the nominal as-received ME3 microstructure is shown in Figure 1. The microstructure of the as-received material consisted of γ grains approximately 4 to 5 μm in size. Observed within the γ grains were primary γ′ particles approximately 2 μm in size

along with secondary γ' particles that exhibited a wide range in size. Table I indicates the nominal compositions of the alloys used for this study.

Figure 2 illustrates the solvus approach curve—the equilibrium γ' solvus temperature as a function of temperature—that had been obtained previously for Rene'88DT[11] and ME3.[30] It is noted from these works that the gamma prime solvus temperatures for Rene'88DT and ME3 are approximately 1103 °C and 1156 °C, respectively.

B. In-Situ Temperature Control

As means of imposing sufficient control over the heating and cooling of the specimens while performing the XRD experiments, a small air furnace unit with a proportional-integral-derivative (PID) temperature control loop was utilized. The furnace was provided by GE Aviation and is a common design constructed out of insulating material and SiC ignitor heating elements encased in sheet metal housing. Port holes were machined into the insulation material to allow for uninterrupted passing of the incident and diffracted X-ray beam. A schematic of the furnace unit is shown in Figure 3(a).

The temperature control was implemented using a Type-R thermocouple that was tack-welded on a fixture composed of Rene' N5 superalloy material that positioned the specimen. The γ' solvus temperature of Rene' N5 has been reported to be 1270 °C[31] which is approximately 93 °C higher than that supersolvus heat treat temperature applied to the ME3 alloy. This served to minimize any temperature effect from the Rene' N5 γ' precipitation within the control signal. An additional Type-R thermocouple was tack-welded to the top of each specimen to allow for direct measurement of the specimen temperature. A Type-K thermocouple probe was inserted below the sample to confirm the temperature uniformity of the furnace environment during the experiments. A photograph of a specimen in the fixture is shown in Figure 3(b).

C. In-Situ Temperature Experiments

1. On-cooling precipitate evolution

In order to assess the γ' response of the Rene'88DT and ME3 alloys in-situ during cooling from solution temperatures, a series of controlled continuous cooling experiments were performed while diffraction pattern measurements were collected for the duration of the thermal cycles. Prior to the on-cooling measurements, the samples were heated to the solution temperature at a rate of 28 °C/min and held at their respective solution temperatures for 1 hour. The solutioning temperatures applied to ME3 and Rene'88DT were 1177 °C and 1165 °C, respectively. Following solutioning, the specimens were cooled at a controlled rate of 28 °C/min to room temperature. The thermocouple data obtained from these trapezoidal temperature profiles including the
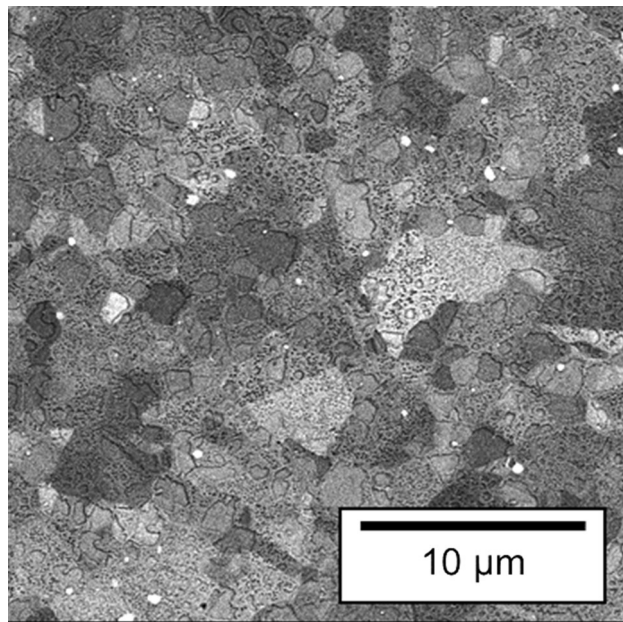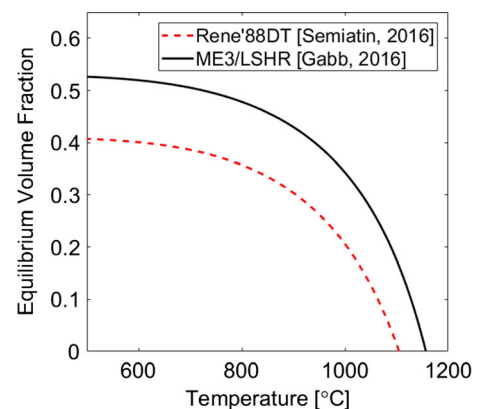

Fig. 1—Backscatter Electron Micrograph (BSE) image of the as-forged ME3 input microstructure obtained using a Tescan Mira3 FEG-SEM at a 10 mm working distance and accelerating voltage of 5 kV.

Fig. 2—Equilibrium γ' volume fraction plotted as a function of temperature—also known as the solvus approach curve—for the Rene'88DT and ME3 alloys.

Table I. Nominal Alloy Compositions for ME3 and Rene'88DT

Alloy	Ni	Co	Cr	Mo	W	Nb	Ta	Al	Ti	C	B	Zr
ME3[10,29]	bal.	20.1	14.2	2.25	0.63	0.56	0.75	7.26	4.33	0.25	0.13	0.03
Rene'88DT[9]	bal.	12.8	17.5	2.42	1.23	0.44	0.00	4.28	4.51	0.24	0.08	0.03

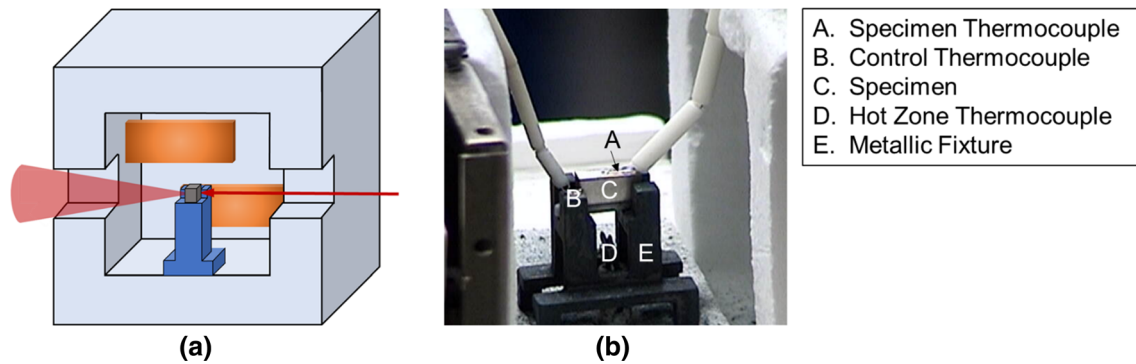Quantities have been converted to at pct.

Fig. 3—Experimental setup of the *in-situ* temperature control used during the synchrotron experiments. (*a*) Schematic view of the air furnace used for the heating and cooling of the sample and path of incident and diffracted X-ray beam. The SiC heating elements are denoted by the orange rectangles embedded in the side walls of the furnace chamber. (*b*) Photograph of a sample in the sample holder within the furnace with the insulation board partially removed.
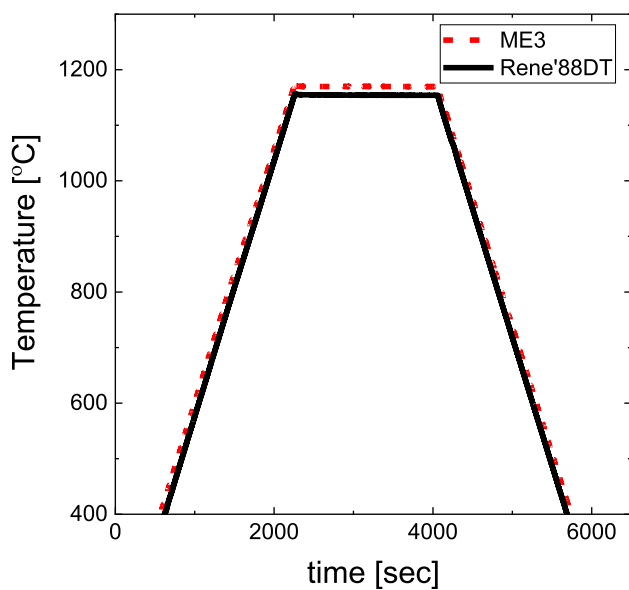

Fig. 4—Trapezoidal temperature profiles used for controlled heating and cooling of the ME3 and Rene'88DT specimen. Both the heat-up and cool-down rates applied to the specimen were 28 °C/min.
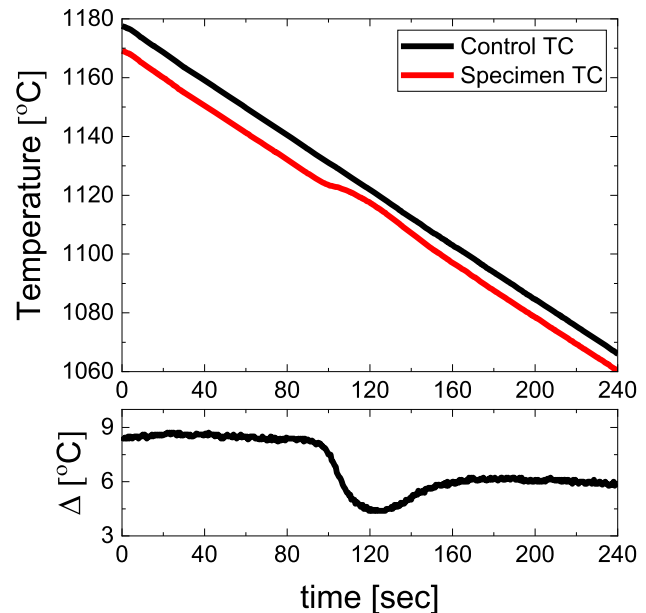

Fig. 5—Plot of cooling profile of the continuously cooled ME3 specimen as measured by the control and specimen thermocouples. The time axis has been adjusted such that $t = 0$ s coincides with the start of continuous cooling from the supersolvus solutioning temperature. The temperature difference between the control and monitoring thermocouples in the lower plot shows a deviation where the onset of the γ' burst exothermic reaction occurs which is approximately 1127 °C.

heat-up, solutioning, and continuous cooling portions are shown in Figure 4 for both alloys.

To independently verify the onset of γ' precipitation during the on-cooling experiments, thermocouple data were recorded for both the control thermocouple and specimen thermocouple to differentiate temperature fluctuations due to the onset of the γ' precipitation with the specimens. The initial on-cooling precipitation event occurs as a nucleation burst that is accompanied by a release of heat. Temperature data recorded as part of the verification are shown in Figure 5 where a calculation of the temperature differential between the control and specimen thermocouples is also shown.

2. Subsolvus isothermal holds

Subsolvus isothermal hold experiments were conducted on a series of ME3 specimens *in-situ* while diffraction data were collected as a means of characterizing the γ-γ' misfit evolution as a function of time at temperature. A total of five temperatures were selected including 1138 °C, 1127 °C, 1053 °C, 998 °C, and 843 °C. Prior to the subsolvus holds, each specimen was heated from room temperature at a rate of 28 °C/min to a solutioning temperature of 1177 °C, held for a minimum of 30 minutes, and cooled to the hold temperature at a rate of approximately 180 °C/min. Shown in Figure 6 are the specimen thermocouple temperature as measured from the start of the rapid cooling sequence. The specimens were held at temperature for a minimum of 30 minutes before allowing to air cool to room temperature.
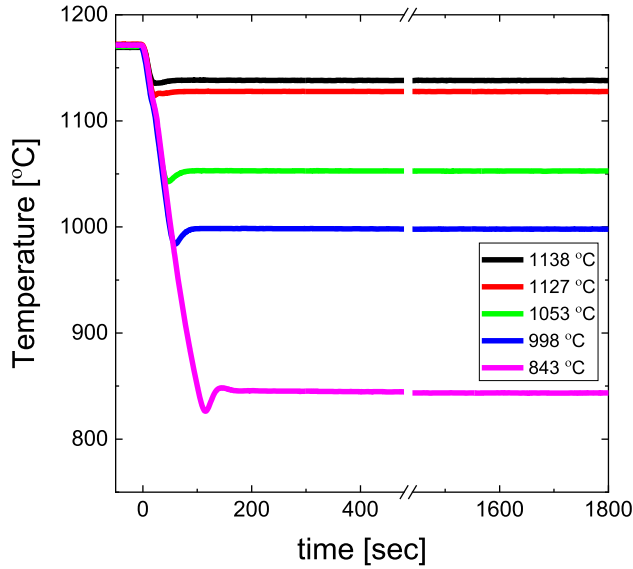
Fig. 6—Thermocouple temperature profiles from the isothermal hold experiments performed on the ME3 alloy. The time axis has been adjusted within the plot such that $t = 0$ seconds coincides with the onset of cooling from the supersolvus solution hold temperature.

D. Synchrotron X-ray Diffraction Measurements

In-situ X-Ray Diffraction (XRD) experiments were carried out using the 11-ID-C Beamline at the Advanced Photon Source at Argonne National Laboratory. A similar overall setup was used for both the continuous cooling and isothermal hold experiments. Each of the specimens were placed approximately 1800 mm away from a Perkin-Elmer 2D area detector with a pixel area of 200 × 200 square pixels. The exact distance was calibrated using a CeO_2 standard for each experimental setup at room temperature. Diffraction pattern data were acquired every 10 seconds. Each pattern was collected automatically using where the thermocouple temperature was recorded within a log file and synchronized with each pattern acquired. Following the pattern collection, each of the 2D files were integrated using the program Fit2D[32,33] to obtain 1D line profiles for subsequent analysis. The X-ray wavelength and angular position obtained from the raw experimental data were translated into reciprocal space represented by the quantity, Q, where Q may be expressed as

$$Q = \frac{4\pi \sin(\theta)}{\lambda}, \qquad [1]$$

where θ is the angle between the direct and diffracted beam and λ is the wavelength of the X-ray source. Following the on-cooling *in-situ* experiments, the 1D line profiles were stitched into a single two-dimensional array of peak intensities arranged in time-order for each specimen. The time series data were translated into temperatures based on the temperature recorded with each pattern.

E. Diffraction Pattern Analysis and Constrained Misfit

1. Intensity ratio determination

As contributions from γ and γ' to the fundamental diffraction peak intensities are difficult to resolve when the misfit is small, a procedure was adapted from[27] in order to evaluate the γ/γ' lattice parameter evolution from the diffraction patterns as function of temperature. Starting from the general relationship between experimental parameters and diffracted peak intensity[34] and accounting for volume fraction of each of the phases, one can obtain the ratio[35]

$$\frac{I^{\gamma'}_{(hkl)}}{I^{\gamma}_{(hkl)}} \propto \frac{\left| F_{(hkl)} \right|^2_{\gamma'}}{\left| F_{(hkl)} \right|^2_{\gamma}} \frac{V_{f_{\gamma'}}}{V_{f_{\gamma}}}, \qquad [2]$$

where $I_{(hkl)}$ and $F_{(hkl)}$ are the integrated intensity and structure factor of the atomic plane (hkl) for the γ' and γ phases, respectively, and V_f is the volume fraction for of each the phases. For intensity ratios consisting of overlapping peaks at a single angular position, it was assumed that temperature-dependent thermal vibrations and their contribution to the atomic scattering factor could be neglected as the effect would be the same for both phases being evaluated. The analytical form of the structure factor for γ' base consisting of a $L1_2$ structure may be expressed as[35]

$$F^{\gamma'}_{(hkl)} = \sum_{\alpha} c_{\alpha} f_{\alpha} \left[e^{\pi i(h+k)} + e^{\pi i(k+l)} + e^{\pi i(h+l)} \right] + \sum_{\beta} c_{\beta} f_{\beta}, \qquad [3]$$

where the subscripts α and β are, respectively, denote the elements at the face-center and simple cubic lattice sites, c is the fractional site occupancy of the sublattice site, and f is the atomic scattering factor of the sublattice site. Similarly, the structure factor for the γ phase consisting of a face-centered cubic (FCC) structure may be expressed as[35]

$$F^{\gamma}_{(hkl)} = \sum_{Z} c_Z f_Z \left[1 + e^{\pi i(h+k)} + e^{\pi i(k+l)} + e^{\pi i(h+l)} \right], \qquad [4]$$

where z is used to denote the element at A1 cubic sites. In the present study, estimates of the temperature-dependent structure factors of the γ and γ' phases are accomplished using CALPHAD-based thermodynamic modeling as described in the following section.

2. Thermodynamic modeling

To assess the compositional effects on phase volume fraction and lattice site occupancies with temperature on the overall diffraction peak intensity ratios, thermodynamic modeling of the alloy compositions at each temperature of interest was performed. This was accomplished using Thermo-Calc 2019b with the TCNI9 thermodynamic database.[36] The phases included in the model were γ, γ', MC, $M_{23}C_6$, $M_{12}C$, and M_6C phases while all other phases were suspended. The equilibrium cite occupancy calculation within the ther-

modynamic model relies on a unified definition of the Gibbs Free Energy across phases and sights and an optimization process determines the lowest energy configuration. Tables II and III summarize a comparison of the Thermo-Calc phase composition predictions to experimental data obtained by Gabb, et al, for ME3[30] and Rene'88DT,[37] respectively. For a basis of comparison, the single-point equilibrium Thermo-Calc predictions were obtained at 600 C.

It is noted that there are some discrepancies in the thermodynamic predictions of the phase compositions and those obtained from experiment. Namely, appreciable discrepancies—larger than 15 pct absolute difference—are predominately associated with the quantities of the minor elements for each of the phases. It is also noted, however, that the influence of the thermodynamic modeling prediction on the subsequent structure factor calculation and overall intensity ratio remains limited when compared to the effect from the change in γ' volume fraction. This is because the overall change in atomic site occupancy contributes to less than 10 pct variation in the relative intensity, whereas the variation attributed to volume fraction change over the temperature range of interest is higher by an order of magnitude.

For the analysis, the atomic scattering factor is obtained from elemental reference data for the appropriate X-ray energy range of the experiment.[35] The thermodynamic model predictions were then incorporated into analytical expressions for structure factor described previously. Figure 7 illustrates the changing intensity contributions for three different γ' volume fractions—0.05, 0.25, and 0.50—for the ME3 composition.

3. Intensity profile analysis and lattice parameter determination

Following the structure factor calculations, the lattice parameter determination and lattice misfit between the γ and γ' phases were performed using the method proposed by Stone et al.[25] The overall procedure was divided into three steps: (1) determination of the γ' lattice parameter, (2) proportioning of the fundamental reflection intensities, and (3) deconvolution and lattice parameter determination of the γ phase. Peak-fitting for each of the steps was achieved using the LIne PRofile Analysis Software package, LIPRAS.[38]

For the first step, pseudo-Voigt functions were fit to the (100), (110), and (211) superlattice reflections of each integrated profile to determine their angular position and lattice parameter obtained from the d-spacing of the peaks and averaging over these peaks. For the second step, a single pseudo-Voigt function was fit to each of the (200) and (220) fundamental reflections to determine the overall integrated peak intensity. The overall peak intensity was then proportioned based on the relative intensity contribution of the two phases based on the thermodynamic modeling results obtained previously. For the final step, the lattice parameter of the γ phase was then deconvoluted from the (200) and (220) fundamental reflections by fixing the angular position

of the γ' phase obtained in the first step and constraining the relative intensity contributions of each phase obtained in the second step. Pseudo-Voigt functions with the same Full Width Half Max (FWHM) for the γ and γ' phases were also prescribed for each reflection. The peak position of the γ phase for each reflection was obtained by optimizing the goodness of fit of the overall intensity under the constraints imposed. The γ lattice parameter was then obtained by averaging the calculated lattice parameters obtained from the d-spacings of the deconvoluted peak positions.

While not included in the deconvolution procedure, the (331) peak is a higher angle peak which is more sensitive to lattice parameter changes and therefore potentially more suitable for observing variation. For a qualitative assessment of the peak position—and therefore lattice parameter—and its change with temperature, contour plots of the (331) peak as a function of temperature are rendered for each of the alloys studied for the data collected during the continuous cooling experiments.

4. Lattice misfit calculation

The constrained misfit between the γ and γ' lattices within the specimens was quantified as a function of temperature and compared across the two alloys for the on-cooling experiments. The constrained misfit, δ, was calculated using the following expression[39]:

$$\delta = \frac{2(a_{\gamma'} - a_\gamma)}{(a_{\gamma'} + a_\gamma)}, \qquad [5]$$

where $a_{\gamma'}$ is the γ' lattice parameter and a_γ is the γ lattice parameter. While the constrained misfit quantity is generally applicable for the cases of fully coherent precipitates embedded within a matrix, it is noted that the significance of this quantity can diminish as coherency is lost. In such cases, the use of unconstrained misfit may be more representative. For a basis of comparison within this study, constrained misfit is considered in the context of the continuously cooled experiments and a more general comparison of lattice parameter quantities is used for assessing the evolution observed during the isothermal experiments.

5. Microstructure characterization

Following the experiments, the subsolvus isothermal hold specimens were mounted and polished using standard metallographic techniques with a final vibratory polish using a colloidal silica suspension. Electron backscatter diffraction (EBSD) was used to identify grains that were oriented such that the polish plane normal was parallel to the $\langle 100 \rangle$ which was performed using a JEOL JSM-6610 with a tungsten filament equipped with an Oxford Instruments HKL Nordlys system collected using an accelerating voltage of 15 kV. Backscattered electron images of the identified grains were obtained using a Hitachi SU-70 Field Emission SEM operated at an accelerating voltage of 7 kV. Three grains from each specimen were characterized as part of the analysis. Image analysis was performed to obtain

Table II. A Comparison of Measured and Predicted Phase Composition Performed for on the ME3 Composition Space

Source		Ni	Co	Cr	Mo	W	Nb	Ta	Al	Ti	C
Experiment[30]	alloy comp.	bal.	20.5	14.35	2.23	0.65	0.496	0.764	7.18	4.6	0.254
	γ	34.28	31	27.31	3.86	0.78	0.11	0.05	2.09	0.5	—
	γ'	63.6	10.07	2.01	0.81	0.52	0.97	1.42	12.1	8.27	—
TCNI9	γ	30.6	34.7	28.6	4.3	1.35	0.05	0.02	0.48	0.07	5.00E-06
	γ'	66	8.7	0.7	0.3	0.05	0.9	1.4	13.1	8.7	1.00E-06

The experimental work was performed by Gabb et al.[30]

Table III. A Comparison of Measured and Predicted Phase Composition Performed for on the Rene'88DT Composition Space

Source		Ni	Co	Cr	Mo	W	Nb	Ta	Al	Ti	C
Experiment[37]	alloy comp.	bal.	12.8	17.8	2.42	1.27	0.44	—	4.5	4.5	0.242
	γ	52.3	16.7	24.3	2.93	0.89	0.13	—	1.96	0.86	—
	γ'	65.7	10.3	3.50	1.55	1.68	1.11	—	4.36	11.70	—
TCNI9	γ	47.8	18.3	27.8	3.49	2.00	0.00	—	0.48	0.08	5.00E-06
	γ'	70.6	4.30	0.70	0.05	0.05	1.16	—	11.3	11.80	1.00E-06

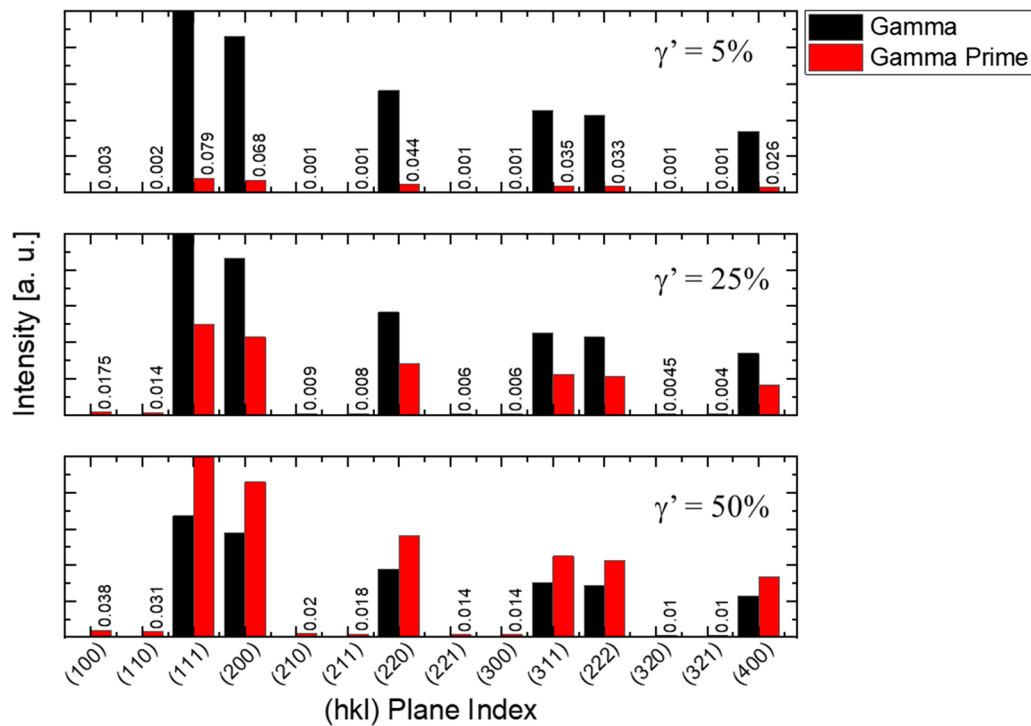The experimental work was performed by Gabb et al.[37]

Fig. 7—Normalized relative intensities of the γ and γ' phases based on structure factor change using the site occupancies predicted by the thermodynamic model data. The plane indices are shown along the horizontal axis. Each subplot represents a different γ' volume fraction and the corresponding change in relative intensity. The numerical values within the graphs denote the smallest, non-zero relative intensity quantities.

area fraction measurements of the γ' phase for each of the conditions. The averaged results are presented and compared to the equilibrium γ' volume fraction as presented by Gabb et al.[30]

6. Precipitation model comparison

To illustrate a comparison between the superlattice peak evolution as a function of temperature and the general precipitate evolution during the continuous cooling experiments, a mean-field precipitation model is employed. The precipitation model, originally proposed for modeling the precipitation of Rene'88DT by Gabb et al.,[21] which has also been subsequently been generalized and applied to other alloys[40] is selected for this study. For this work, the modeling was performed for the Rene'88DT composition by using the calibration data proposed by Semiatin et al.,[11] and imposing a linear cooling rate of 28 °C/min within the calculation. The instantaneous volume fraction was then compared to the profile obtained from (100) superlattice peak

intensity as a function of temperature after it has been normalized by the incident beam intensity for each pattern collected.

III. RESULTS

The experimental results for the *in-situ* experiments are presented in the following sections. Observations obtained directly from the diffraction pattern data for the ME3 and Rene'88DT alloys are presented, followed by a comparison of the calculated misfit obtained from the deconvolution procedure. For the ME3 alloy, a comparison of the continuous cooling and the isothermal lattice parameter measurements is presented. Also for the ME3 alloy, the microstructure observations obtained from the subsolvus isothermal specimens and corresponding phase fraction measurements are presented.

A. *Peak Deconvolution*

An example diffraction pattern acquired for the ME3 alloy at 600 °C during the continuous cooling experiment is shown in Figure 8 annotated with the superlattice peaks ((100), (110), and (211)) and fundamental peaks ((200) and (220)) used for the deconvolution procedure.

Figure 9 illustrates an example of the deconvolution results for the (200) and (220) fundamental peaks of the ME3 alloy at 600 °C. Shown in each of the plots is the total peak intensity, background fit, constrained γ' phase intensity contribution, and the deconvoluted γ phase intensity contribution.

B. *On-Cooling Lattice Parameter and Constrained Misfit vs Temperature*

1. *Lattice parameter vs temperature*
Figures 10(a) and (b) illustrate the lattice parameter change with temperature for the γ and γ' phases for the
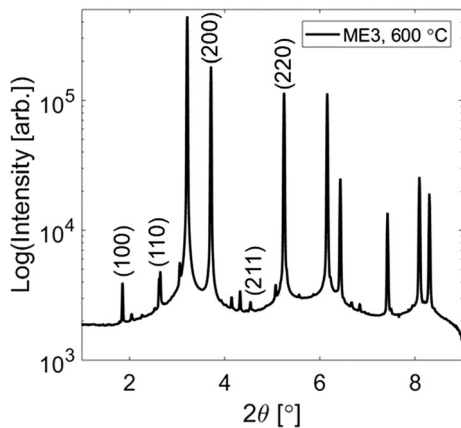

Fig. 8—An example diffraction pattern acquired for the ME3 alloy at 600 °C during the continuous cooling experiment annotated with the superlattice peaks ((100), (110), (211)) and fundamental peaks ((200) and (220)) used in the deconvolution procedure.

ME3 and Rene'88DT alloys for the on-cooling experiments, respectively. Evident in the plots of lattice parameters are intersections where the γ' phase transitions from having a smaller lattice parameter than the γ phase to it having a larger lattice parameter. This transition occurs between 850 °C and 800 °C for the ME3 alloy. A similar transition is noted as occurring between 750 °C and 700 °C for the Rene'88DT alloy.

2. *Constrained misfit vs. temperature*
The deconvoluted lattice parameter results were used directly to calculate the constrained γ/γ' misfit quantities. The quantitative results of the misfit analysis are present for ME3 and Rene'88DT in Tables IV and V, respectively. Figure 11 illustrates a comparison of the ME3 and Rene'88DT misfit trends as a function of temperature during the on-cooling experiments. The largest negative misfit for both alloys can be observed at temperatures nearest the respective γ' solvus temperatures. Both alloys exhibited overall a monotonic variation of misfit with decreasing temperature, with near-zero values at intermediate temperature, and positive values at lower temperature. The overall magnitude in misfit at 600 °C for ME3 is approximately twice that observed for the Rene'88DT alloy.

3. *Superlattice peak characteristics vs temperature*
Figures 12 and 13 illustrate, respectively, the changes to the (100) superlattice peak characteristics as a function of temperature for the ME3 and Rene'88DT alloys. As shown, the largest magnitude of change to the peak characteristics—in terms of peak position, width, and normalized intensity—coincides with the specimen temperature change associated with the secondary γ' burst event. This temperature is approximately 1127 °C for ME3 and 1067 °C for Rene'88DT and is denoted by the roman numeral, II, within the figures. Subsequent changes to the superlattice peak characteristics vary between the alloy compositions. For the ME3 alloy, there is a discontinuity within the superlattice peak position as it varies with temperature that occurs between approximately 925 °C and 850 °C. The onset of variation observed in the other superlattice peak characteristics is also consistent with this. For the case of the Rene'88DT alloy, no such change to the superlattice peak position was observed, however, discontinuities in the normalized peak intensity may be observed beginning at approximately 815 °C. These fluctuations are attributed to the tertiary γ' burst events for the two alloys and is denoted by the roman numeral, III, within the figures.

C. *Diffraction Pattern Line Profile vs. Temperature*

As an additional measure of evaluation, the peak intensity contours of the integrated 1D data for ME3 and Rene'88DT for all of the peaks within the angular range of the acquired data collected are shown in Figures 14(a) and 15(a), respectively, where the (331) peak is denoted by a vertical arrow. Figures 14(b) and 15(b) show the intensity change of the (331) fundamental peak for each alloy as a function of temperature and
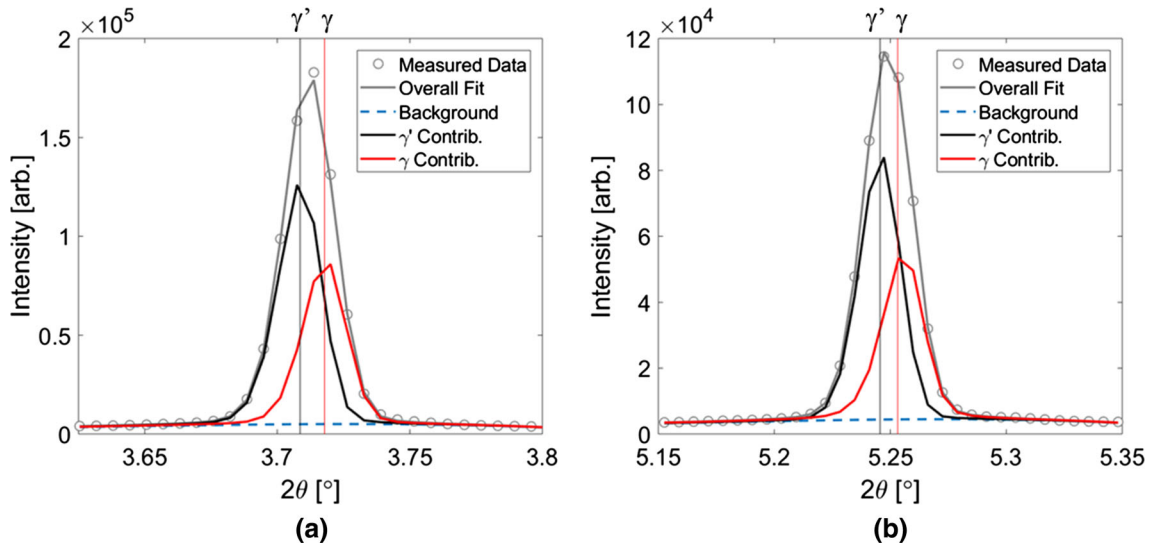
Fig. 9—Isolated and deconvoluted fundamental diffraction peak obtained from diffraction data for ME3 collected at 600 °C during the continuous on-cooling *in-situ* experiments. (*a*) Corresponds to the (200) fundamental peak and (*b*) corresponds to the (220) peak. Also shown are the approximate peak positions for the phases as well as the background level and total peak intensity.
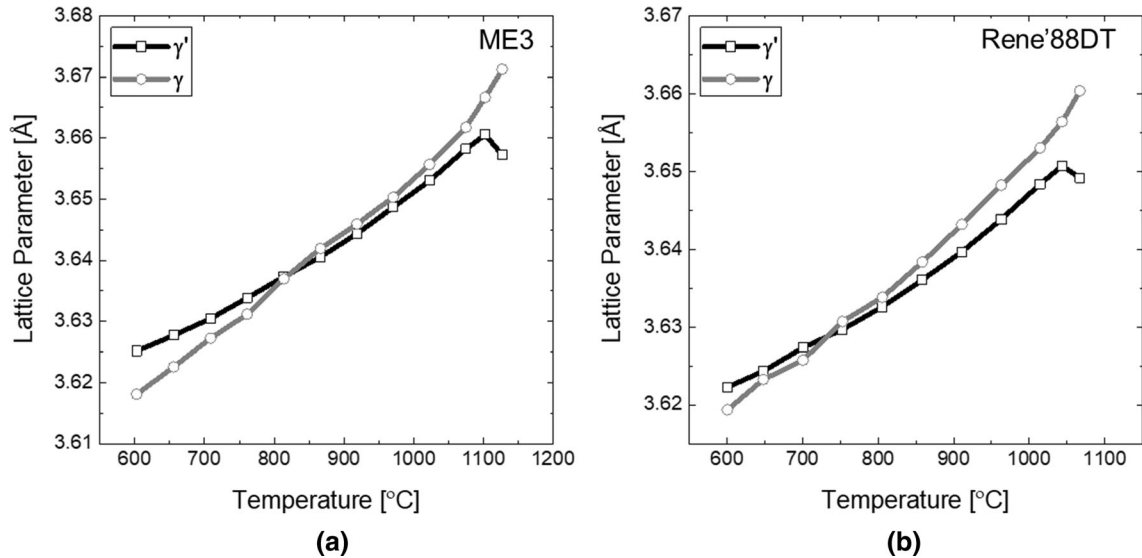

Fig. 10—Lattice parameter for the γ and γ' phases plotted as a function of temperature for the (*a*) ME3 and (*b*) Rene'88DT alloys. The data were obtained from X-ray Diffraction patterns collected *in-situ* during continuous on-cooling experiments.

the reciprocal space quantity, Q. As shown, the Q-value of the peak increases with decreasing temperature which corresponds to a decrease in lattice parameter. This general observation is consistent with thermal contraction of the volume as the thermal energy is decreased. Also denoted within the (331) intensity contour subplots are perturbations attributed to the γ' burst response starting at 925 °C for ME3 and 815 °C for Rene'88DT. These are consistent with the temperatures denoted in the superlattice peak characterization presented previously. For the Rene'88DT alloy, the γ' precipitation event occurs at a lower temperature which is consistent with the shift in γ' solvus temperature between the two

alloys. The proposed secondary (II) and tertiary (III) burst start temperatures are annotated within Figures 14 and 15 for ME3 and Rene'DT, respectively. Additional peak shape information near the onset temperature of the tertiary burst event as observed within the (331) peak is presented in Figures 14(c) and 15(c) for ME3 and Rene'88DT, respectively. With decreasing temperature additional intensity fluctuations were observed for both alloys. The range of intensity fluctuations for the ME3 alloy was between 950 °C and 800 °C while the fluctuations for the Rene'88DT alloy were observed between 850 °C and 600 °C.

D. Precipitation Modeling and Superlattice Profile Comparison

Figure 16 illustrates the instantaneous γ' volume fraction predicted by the precipitation model compared to the normalized superlattice peak intensity as a function of temperature for the Rene'88DT composition. Also shown is the equilibrium γ' volume fraction change with temperature as determined by Semiatin et al.[42] After the initial γ' burst between 1072 °C and 1067 °C, the instantaneous volume fraction rapidly approaches the equilibrium volume fraction. This trend is mirrored by the increase in the superlattice peak intensity and continues until the onset of a subsequent burst event at approximately 800 °C where an inflection point within both the instantaneous volume fraction and superlattice peak intensity can be observed.

E. Isothermal Hold Experiments

1. Temperature-dependent lattice parameter comparisons

Figure 17(a) illustrates the lattice parameters for the γ and γ' phases obtained from the data collected as part of the isothermal hold experiments. As shown, the largest difference in lattice parameter between the two phases is nearest to the γ' solvus temperature and converges monotonically with decreasing temperature. Shown in Figure 17(b) is the comparison of the γ' lattice parameter change with temperature for the on-cooling experiment and the isothermal hold experiments for the ME3 alloy. The data plotted for the isothermal hold experiments correspond to the time points where the specimens were held at temperature for 30 minutes. As shown, the misfit values are similar between the instantaneous on-cooling misfit response and the misfit after 30 minutes at temperature. The two experiment types (continuous cooling and isothermal) show similar quantities for observed γ' lattice parameters for the conditions evaluated with the largest measured difference occurring at 1127 °C.

2. Isothermally exposed microstructure characterization

SEM characterization of the specimens after the subsolvus isothermal holds were used to elucidate the γ' morphology. Figure 18 shows the BSE images obtained for four of the subsolvus isothermal hold conditions including 1138 °C, 1127 °C, 1053 °C, and 998 °C. All images shown have a plane normal axis that is within 3° of the ⟨100⟩ direction. As shown for the two higher temperatures, 1138 °C and 1127 °C, a bimodal distribution of the γ' precipitates can be observed. The smaller γ' precipitates for these two conditions are attributed to the continued evolution of the γ' volume fraction with decreasing temperature resulting in subsequent burst events.

Table VI summarizes the gamma prime area fraction measurements obtained for the γ' populations that formed at the target hold temperatures and a comparison is made to the expected equilibrium volume

fractions, estimated from,[30] for each of the conditions. It is noted that the measured γ' area fractions of the γ' associated with the isothermal hold are higher than those predicted by other work, particularly for the case of the 1127 °C specimen. The possible reasons for this is subsequently discussed.

IV. DISCUSSION

A. Procedural Influences on Lattice Parameter and Misfit Quantification

1. Experimental conditions

The degree of uncertainty in the results obtained that could be attributed to the experimental setup including temperature resolution and thermal expansion are considered within this section. At the start of the continuous cooling portion of thermal profile, it can be noted from the y-axis in Figures 14 and 15 that the starting temperature as measured by the control thermocouple mounted next to the specimens and the thermocouple attached directly to the specimens shows some degree of variation. As noted, this temperature difference was approximately 8 °C for the ME3 experiment and approximately 1 °C for the Rene'88DT experiment. This may serve to conservatively bound the expected range of temperature variation nearest to the specimens during each of the experiments which may in turn affect the accuracy of the reported temperatures. It should be noted, however, that the region within the specimens where incident beam passes is positioned close to the center of the specimen and is 0.5 mm in diameter and the temperature range over the interrogated volume is expected to be uniform and closer to the temperatures measured on the specimens themselves.

During the experiments, the furnace, metallic fixture, and specimen all are anticipated to expand and contract with increasing and decreasing temperatures. At a minimum, this is expected to change the location of the incident beam within a given specimen as data are collected. This can result in a change to the diffraction pattern as in a new position the diffracted beam interacts with a different region of the material and the grain orientations that satisfy the Bragg condition. Figures 14(c) and 15(c) serve to illustrate the observed variation in the integrated peak intensities with changing incident location based on temperature change. As shown, the profile is relatively insensitive to temperature-dependent fluctuations outside of the range of γ' burst events. Regarding the effects of any lateral movement—contributing to a change in specimen-to-detector distance—from thermal expansion or contraction, a conservative estimate can be made by calculating the maximum position uncertainty due to thermal expansion. Using a representative thermal expansion value for nickel-base superalloys of 0.025 mm/mm at 1200 °C [41] directly, the corresponding uncertainty in specimen-to-detector distance for the nickel superalloy specimen holder approximately 25 mm in size is ± 0.64 mm, or 0.04 pct of the overall specimen-to-detector length.

Table IV. Summary of Lattice Parameters and Constrained Misfit Results as Determined for ME3

Temperature [°C]	γ' Lattice Parameter [Å]	γ Lattice Parameter [Å]	δ, Constrained Misfit [Pct]
1127	3.657	3.671	− 0.382
1103	3.661	3.667	− 0.166
1075	3.658	3.662	− 0.097
1023	3.653	3.656	− 0.073
971	3.649	3.650	− 0.044
919	3.644	3.646	− 0.043
866	3.641	3.642	− 0.039
814	3.637	3.637	0.009
761	3.634	3.631	0.074
709	3.630	3.627	0.090
656	3.628	3.623	0.141
603	3.625	3.618	0.195

Table V. Summary of Lattice Parameters and Constrained Misfit Results as Determined for Rene'88DT

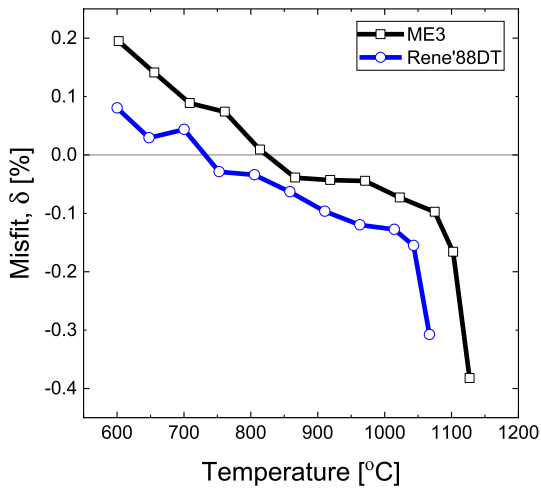| Temperature [°C]	γ' Lattice Parameter [Å]	γ Lattice Parameter [Å]	δ, Constrained Misfit [Pct]
1067	3.650	3.660	− 0.297
1043	3.651	3.656	− 0.137
1015	3.649	3.653	− 0.116
963	3.644	3.648	− 0.107
911	3.640	3.643	− 0.084
858	3.637	3.638	− 0.050
805	3.633	3.634	− 0.021
753	3.630	3.631	− 0.017
700	3.628	3.626	0.056
648	3.625	3.623	0.041
600	3.623	3.619	0.091

Fig. 11—Constrained lattice misfit between the γ and γ' phases plotted as a function of temperature for the two alloys observed within this study, ME3 and Rene'88DT, during continuous cooling *in-situ* X-ray Diffraction experiments.

2. Data refinement

Regarding the peak refinement process, it has been observed by Huang *et al.*,[42] in a neutron diffraction study that the uncertainty of misfit measurement applied to nickel superalloy compositions is about 0.1 pct. This uncertainty is not based on refinement errors but values from repeated measurements. For the current study, we chose a peak-deconvolution method over the whole pattern refinement methods because the latter, either LeBail or Rietveld, seek global minimum and will not be able to handle the weaker superlattice peaks appropriately. Based on these observations, a procedure was selected for this work that relies on averaging of several superlattice peaks to determine an appropriate quantification of the γ' lattice parameter at each measurement point. A k-factor-based 95 pct Confidence Interval[43] of the average γ' lattice parameter ranges from ± .002 Å to ± 0.012 Å for the patterns measured during the on-cooling experiments. For the specific case of the ME3 alloy measured at 600 C, the range in γ' lattice parameter was found to be ± 0.008 Å which translates to a misfit uncertainty of ± 0.004, or 2.23 pct of the reported value.

The degrees of freedom of the refinement process applied within the present study are limited by direct knowledge of superlattice peak positions and their relatively small change with angular position over the observed angular range. Assuming the same FWHM peak width for the two phases also serves to constrain the solution space. This assumption is based on the existence of an approximately equivalent coherent length of the two adjacent phases, or more specifically, the γ channel width between γ' particles is similar in size
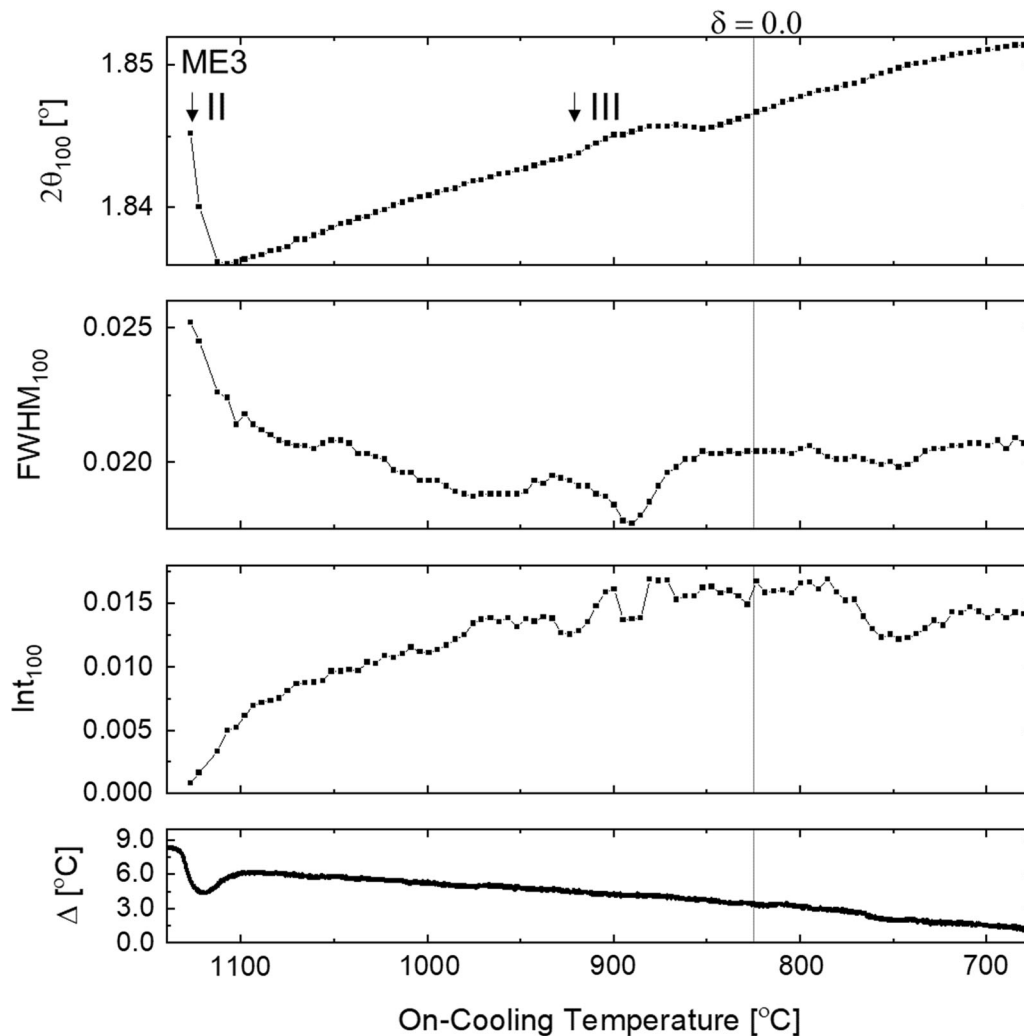
Fig. 12—(100) Superlattice peak characteristics plotted as a function of on-cooling temperature for the continuous cooling *in-situ* experiments performed on ME3. Shown in the subplots arranged from top to bottom are peak position, peak FWHM width, and normalized peak intensity. The bottom subplot of the figure shows the specimen thermocouple temperature difference when compared to the control thermocouple temperature to indicate temperature regimes associated with the γ' burst event. Also shown in all of the subplots is a vertical reference line indicating the transition from negative to positive misfit as determined from the on-cooling experiments.

to the size of the γ' particles themselves. This assumption is sensitive to the average γ' size at the time of the measurement and may be less accurate when the γ' size is smallest at the initial burst temperature. Inspection of the FWHM for the (100) superlattice peaks presented in Figures 12 and 13 for ME3 and Rene'88DT, respectively, suggests that the average superlattice peak width is relatively constant after the initial burst has occurred.

B. Secondary and Tertiary γ' Response during Continuous Cooling

1. Differential thermal response

The thermal response of the γ' evolution provides an additional measure to correlate the observed diffraction pattern changes. The γ-γ' transformation is a first-order phase transformation that releases energy in the form of heat into the surrounding material. This phenomenon has been observed using conventional Differential Thermal Analysis (DTA) techniques[6,20,44] where the latent

heat release rate is observed to be proportional to rate of volume fraction change with time. Generally, this results in higher cooling rates producing a higher degree of latent heat. This effect is most pronounced during the secondary γ' burst which can be observed in Figures 12 and 13 where the onset temperatures for ME3 and Rene'88DT were approximately 1127 °C and 1067 °C, respectively. These ranges are consistent with those observed by other works[30,44] for these alloys. These works also suggest that the onset temperature of the on-cooling secondary γ' burst event within γ'-strengthened superalloys is relatively insensitive to cooling rates. Within the present study, the thermal signal was found to be too insensitive to identify additional burst events at temperatures below secondary burst temperatures. While the relative difference between the control temperature signal and the specimen temperature signal for each of the experiments provides a quantitative measure of the onset temperatures, additional calibration efforts
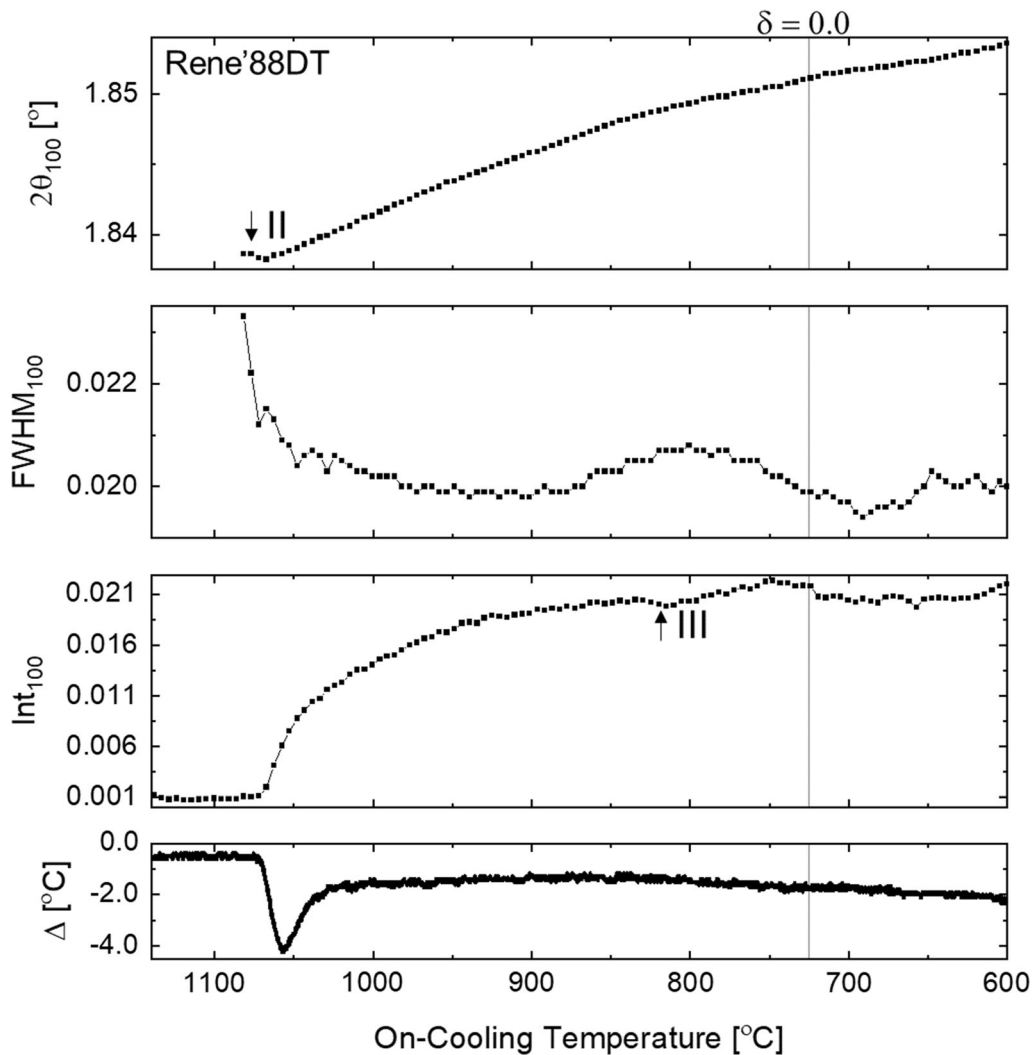
Fig. 13—(100) Superlattice peak characteristics plotted as a function of on-cooling temperature for the continuous cooling *in-situ* experiments performed on Rene'88DT. Shown in the subplots arranged from top to bottom are peak position, peak FWHM width, and normalized peak intensity. The bottom subplot of the figure shows the specimen thermocouple temperature difference when compared to the control thermocouple temperature to indicate temperature regimes associated with the γ' burst events. Also shown in all of the subplots is a vertical reference line indicating the transition from negative to positive misfit as determined from the on-cooling experiments.

would be required to determine a more accurate volume fraction change within each of the alloys associated with the signal.

2. Fundamental peak characterization

The raw diffraction pattern data for the two alloys as shown in Figures 14 and 15 contain two temperature ranges where noticeable changes to the (331) fundamental reflection can be observed. Early in the cooling portion of the temperature profile, both alloys exhibit a sharp, singular discontinuity where the Q-value abruptly changes. This change in the (331) peak with decreasing temperature corresponds to an abrupt change in the phase content due to the secondary γ' burst. During the initial burst, the γ' contribution to the fundamental peak remains low due to the low volume fraction but can be clearly resolved in part due to the small average precipitate size and its correspondence with peak broadening that is observed within the (100) superlattice peak

characteristics for the two alloys as presented in Figures 12 and 13. With lower temperatures, the γ' intensity contribution increases. Despite this, observations of subsequent γ' bursts based on peak width become less pronounced due to the mix of the larger γ' precipitate sizes that formed and grew from higher temperatures. Qualitative changes to the overall peak shape are still observable at lower temperatures, however, and serve as potential evidence of subsequent burst events. The observed perturbations within the fundamental peak widths may be attributable to distortions in the lattice parameters of both the γ and γ' phases that could accompany a phase change event. The range over which these occur appear close to the same range where the lattice misfit between the two phases is low in magnitude, yet non-zero as determined by the peak deconvolution. This range is likely attributable to the γ' tertiary burst and was observed to be between 925 °C and 850 °C for the ME3 alloy. This range is similar to
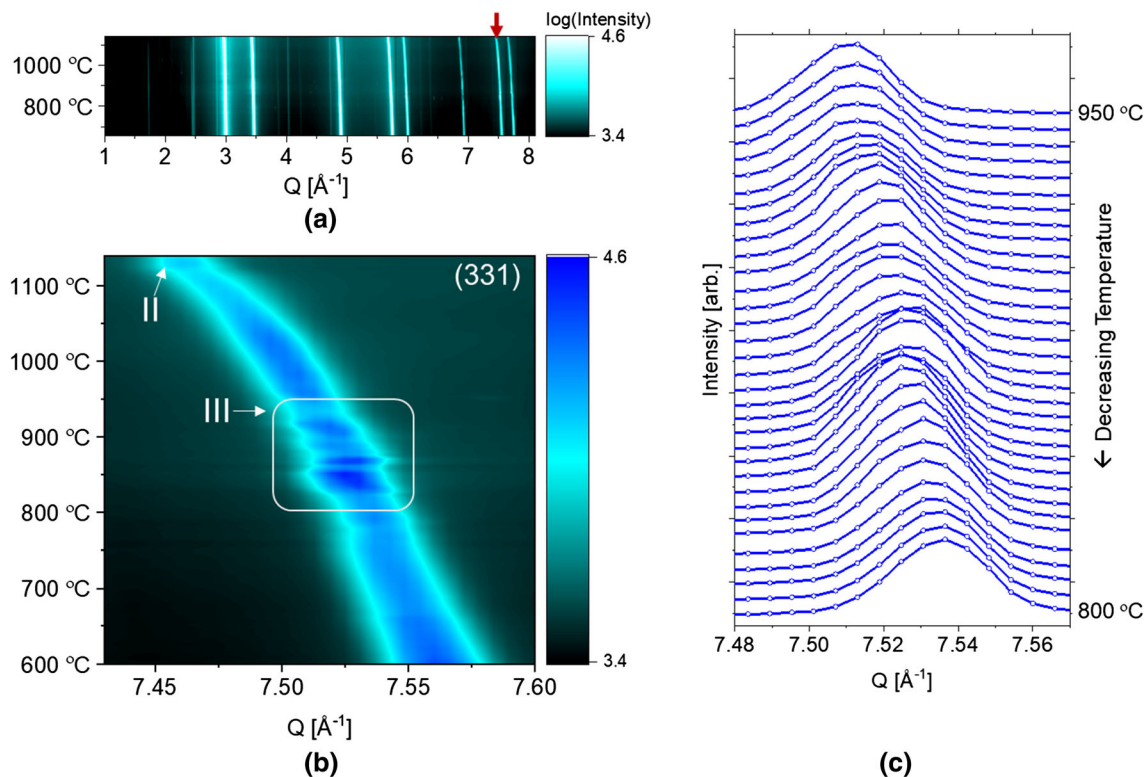
Fig. 14—A composite contour of the 1D line profiles collected for ME3 during the continuously cooled *in-situ* experiment. (*a*) The line profile intensity as a function of temperature on the y-axis and Q-value on the x-axis. (*b*) An isolated view of the (331) profile intensity as obtained from the raw 1D data annotated with the approximate onset points of the secondary (II) and tertiary (III) γ' burst events. (*c*) An intensity-normalized plot of the individual line profiles across the temperature range where intensity fluctuations were observed. The scanning interval between patterns translates to temperature change of approximately 5 °C between the plotted intervals.

the range observed for a similar alloy composition, LSHR, where the burst onset was found to be approximately 907 °C for a different set of experimental conditions and cooling rates.[19]

3. *Deducing γ' precipitation phenomena from superlattice peak characteristics*

Recent work by Collins *et al.*,[45] has demonstrated that multimodal γ' precipitates that form on-cooling from solution follow a nucleation and growth process that can be described under by Classical Nucleation Theory. In this way, the γ' burst events are a balance of thermodynamic driving force, interfacial energy, and temperature-dependent diffusivity. In the case of the tertiary burst, the degree of matrix supersaturation leading up to the burst event greatly depends upon the number density and size of the secondary precipitates that have formed previously.[46] This notional trend can be observed within the precipitation modeling results where the dashed line of Figure 16 representing the instantaneous volume fraction shows the largest deviation from the equilibrium volume fraction trend just before the predicted tertiary burst event. In the context of spatially averaged lattice parameter observations, the results of the current study also suggest that the bulk γ-γ' misfit also differs between the two burst events. Specifically, the difference in average lattice parameter between the two phases is at its largest near the

secondary burst temperature for both alloys. The volume-averaged nature of the synchrotron experimental setup does not provide sufficient sensitivity to other aspects of γ' evolution such as local composition changes, interfacial energy, or local lattice distortion at the matrix–particle interface. More evidence would be necessary to assess the role of misfit on tertiary burst events specifically. These could be performed using *in-situ* diffraction in conjunction with a wider range of cooling rates as well as other methods that could provide *in-situ* compositional information during the experiment.

Prior studies using *in-situ* synchrotron X-ray Diffraction of PM nickel-base superalloys have concluded that multiple tertiary burst events can be deduced from the ratio of a single superlattice peak to a single fundamental peak intensity.[2,47] The challenge with this approach applied to X-Ray patterns occurs when the superlattice peak intensity is very small compared to the fundamental peak intensity as this ratio can be smaller than the uncertainty interval of the fundamental peak intensity. The current study suggests that a full-field view of the peak intensity change with temperature and angular position can provide insight into the tertiary burst phenomena. In terms of direct observations of the superlattice peak intensity, the present study demonstrates interpretable trends for the γ' peak angular position that followed the expected change with
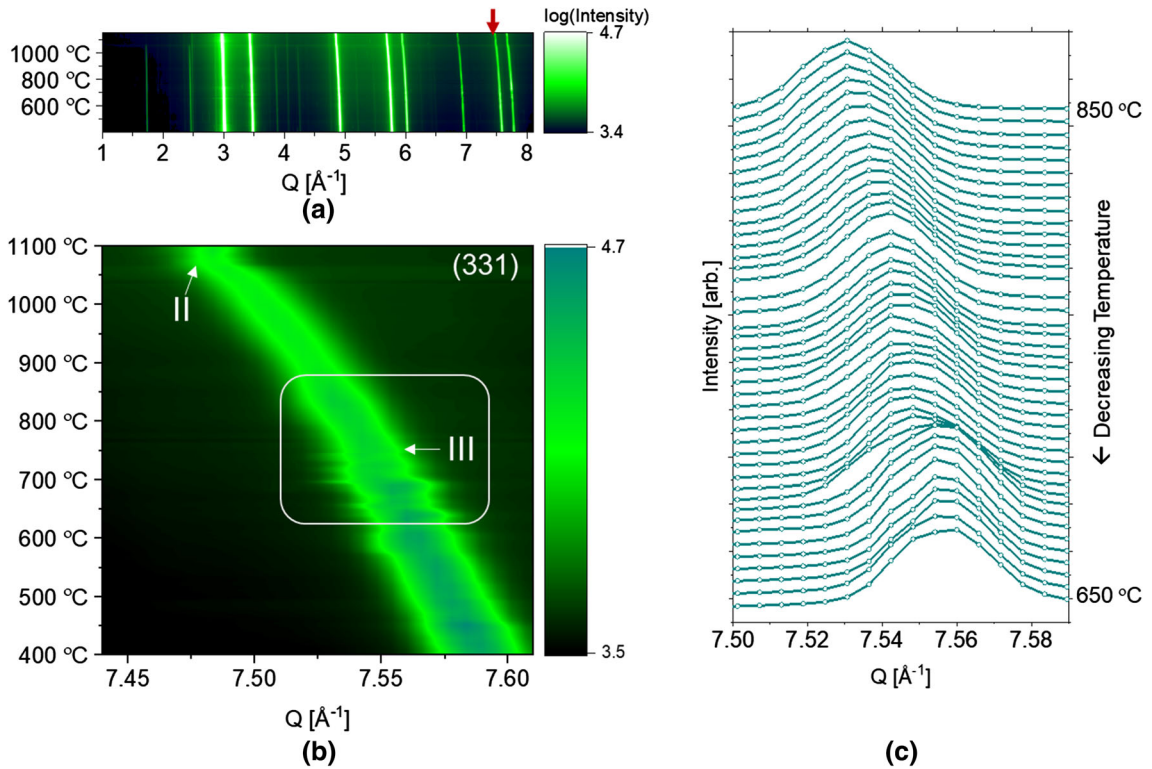
Fig. 15—A composite contour of the 1D line profiles collected for Rene'88DT during the continuously cooled *in-situ* experiment. (*a*) The line profile intensity as a function of temperature on the *y*-axis and *Q*-value on the *x*-axis. (*b*) An isolated view of the (331) profile intensity as obtained from the raw 1D data annotated with the approximate onset points of the secondary (II) and tertiary (III) γ′ burst events. (*c*) An intensity-normalized plot of the individual line profiles across the temperature range where intensity fluctuations were observed. The scanning interval between patterns translates to temperature change of approximately 5 °C between the plotted intervals.
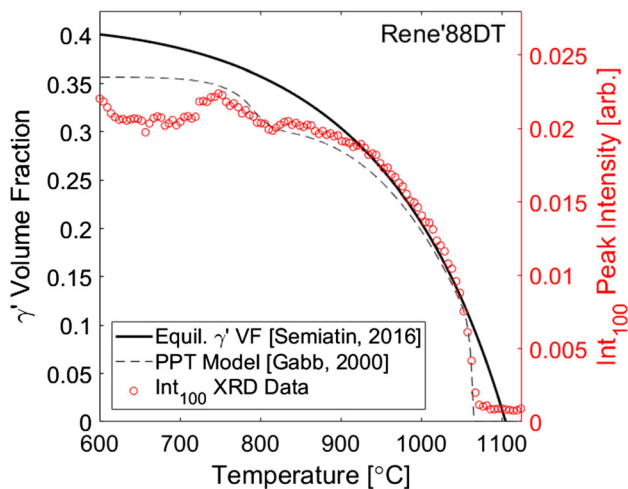

Fig. 16—γ′ precipitation modeling results (left axis) and the (100) superlattice peak intensity variation as a function of temperature (right axis) for the Rene'88DT composition illustrating similarities between the predicted change in volume fraction and the observed change in superlattice peak intensity.

temperature for both alloys. Deviation in these trends can be ascribed to the kinetics of the γ′ burst events where observed. Despite the low relative intensity of the superlattice peaks within the patterns, it may still prove useful for qualitative analyses as presented within this work. Additionally, the comparison of the (100) super-lattice peak intensity as a function of temperature to the instantaneous γ′ volume fraction predicted by a calibrated multimodal γ′ precipitation model also suggests a plausible connection with precipitate evolution and peak intensity.

C. Precipitate Evolution During Isothermal Exposure

The lattice parameter measurements obtained from the XRD experiments of the current study show a consistent trend with the γ′ precipitate morphology determined from the SEM images. As shown in Figure 18, the isothermal hold temperatures result in a range of precipitate shapes. As observed when viewing the grains parallel to the ⟨100⟩, these shapes ranged from a cubic shape with negative curvature at the hold temperature of 1138 °C to near spherical in shape at the hold temperature of 998 °C. It is noted that the number density of γ′ that evolve to these shapes at the target isothermal hold temperature increases drastically across this temperature range and such factors as local solute concentration may inhibit precipitate evolution depending on the level of driving force. The area fraction measurements performed on these specimens suggest that near equilibrium γ′ fractions are likely achieved during the isothermal hold periods of the experiments. Limitations of the *in-situ* setup did not allow for rapid quenching of the specimens after the isothermal
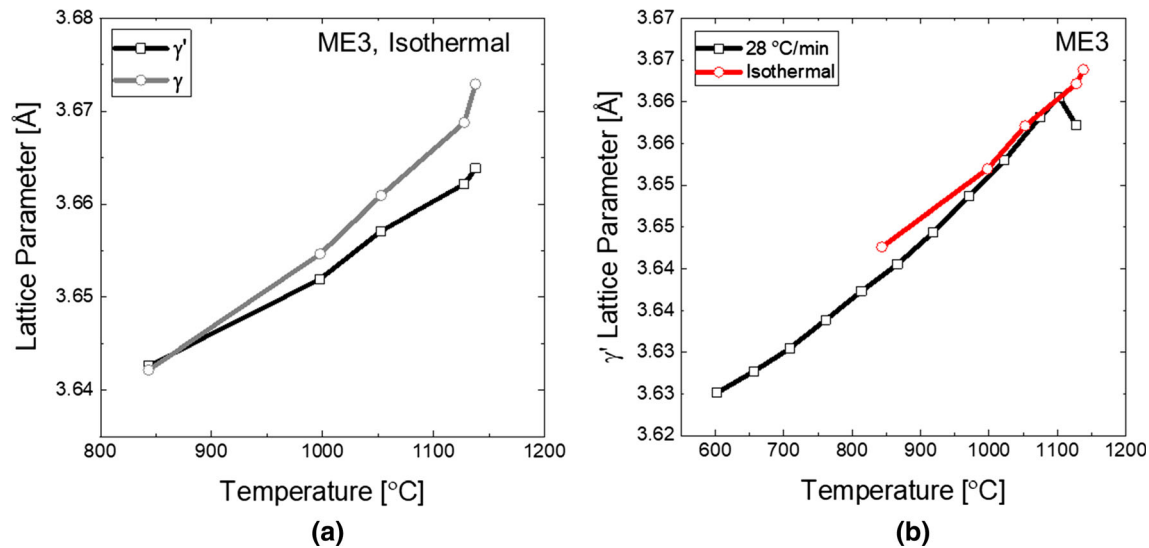
Fig. 17—(*a*) Lattice parameters for the γ (circles) and γ' (squares) phases in ME3 obtained from the isothermal hold experiments. (*b*) Comparison of γ' lattice parameter as a function of temperature obtained for the ME3 alloy for both the continuously cooled (black squares) and isothermal (red circles) experimental conditions (Color figure online).

exposure, thus promoting continued evolution of the precipitates during cooling to room temperature and may serve as a cause for the difference between the experimental equilibrium γ volume fraction reported by others.[42]

The corresponding lattice parameter measurements of specimens show the largest difference at 1138 °C where the precipitates have evolved to the cuboidal shape with negative curvature. This observation and lattice parameter difference supports the expected shape change of the γ' in the context of fully coherent precipitates in the presence of misfit. When the misfit is high, the elastic strain imparted by the misfit during precipitation is anisotropic, promoting growth in the high modulus $\langle 111 \rangle$ direction and faceting along the $\langle 100 \rangle$ direction.[23] This effect decreases with smaller particles and smaller degrees of misfit. The trends observed within this study and the relative change in shape with misfit are consistent with other superalloy precipitate shapes[17] and misfit quantities[22] that have been studied previously.

A comparison of the lattice parameter between the on-cooling and isothermal experiments suggests the compositional change at the temperature nearest the solvus is due to equilibration of the γ' phase. Based on the lattice parameter changes observed within the γ phase, it can be inferred that a compositional change to the γ phase augments this equilibration. This can be rationalized by a comparison of the notional equilibrium phase boundaries for the γ and γ' phases. At higher temperatures, the $\gamma/\gamma + \gamma'$ phase boundary has higher curvature than the $\gamma + \gamma'/\gamma'$ phase boundary which would promote a larger change in composition as the system tends towards equilibrium. As the temperature decreases, there is less deviation between the instantaneous lattice misfit response and the lattice misfit measured after being held at temperature.

D. *Significance of Misfit Within γ'-Strengthened Superalloys*

From the results of the present study, the significance of misfit in terms of its effect on γ' precipitation in γ'-strengthened PM nickel-base superalloys can be discussed. With respect to γ' nucleation, the effect of volumetric strain energy from misfit is likely to be low. This can be deduced from the spherical shape exhibited by the γ' phase in the early stages of evolution as observed when the precipitates are rapidly quenched just after nucleation.[48] The implications of misfit on other stages of precipitate evolution are more likely, however, and are subsequently discussed.

In the context of elastically anisotropic two-phase systems where coherency is maintained, misfit induces orientation-dependent growth that promotes a cuboidal precipitate shape.[24,49] As referenced in the study by Akhlaghi *et al.*,[50] a distinction between two contributions to misfit can be made and applied to the results of the present study. One aspect is related to the differential thermal expansion and contraction of the crystal lattices of each phase with temperature and the other is related to the straining of the lattices due to the volumetric change from the precipitation event itself. As evidenced by the results, the dominate contribution to the misfit observed in the on-cooling experiments appears to be related to the thermal contraction. In terms of the effect of misfit on the micro-elastic lattice distortions that may be present, some qualitative information can be obtained from examining the changes to the superlattice FWHM peak width of Figures 14 and 15 for each of the alloys where it can be observed that the (100) peak is the broadest nearest the secondary γ' burst event. These observations indicate a potential lattice straining at the early stages of γ' evolution where the overall misfit is experiencing a contribution from the precipitation event itself. Due to the elastic anisotropy of the material and
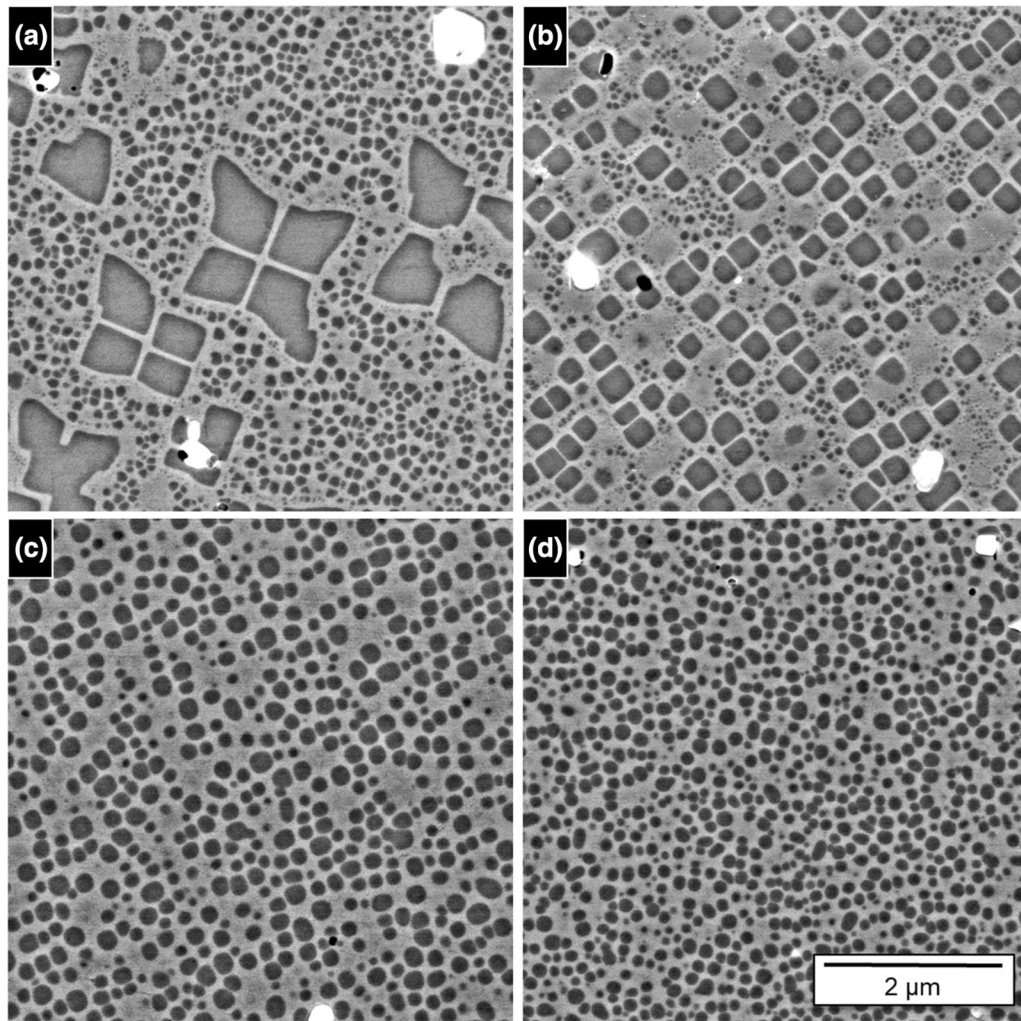
Fig. 18—BSE images of the γ' microstructure of the ME3 alloy following the subsolvus isothermal hold experiments across four of the temperatures. The images are arranged in the order of decreasing temperature where (*a*) 1138 °C, (*b*) 1127 °C, (*c*) 1053 °C, and (*d*) 998 °C. The microstructures of (a), (c), and (d) were obtained following 1 h of the subsolvus isothermal exposure while the microstructure presented in (b) was obtained after 30 min of subsolvus isothermal exposure.

Table VI. Summary of the γ' Area Fraction Measurements Obtained for the ME3 Alloy for the Isothermal Hold Experiments

		Experimental Data	
Exposure Temperature [°C]	Equilibrium γ' Vol. Fraction (est. from[30])	Average γ' Area Fraction	Standard Deviation γ' Area Fraction
1138	0.07	0.12	0.028
1127	0.10	0.28	0.011
1053	0.27	0.32	0.007
998	0.35	0.36	0.016

The area fraction measurements reported have been segmented as to include only the quantity of γ' associated with the isothermal exposure as indicated by the larger size distributions within the images. A comparison the estimated equilibrium volume fraction is also presented.

the potential to form complex precipitate shapes, a more comprehensive analysis would be required to sufficiently evaluate these micro-elastic strain fields that form between the matrix and precipitates.[49]

The results of this study may also suggest that the starting composition has a greater influence in terms of optimizing a desired misfit outcome than what may be controlled by processing. Studies on the alloying effects such as increasing Mo content[14] have been shown to support this conclusion. This is owed to the fact that refractory elements have larger atomic sizes and increase the lattice parameter of the parent phase within which these elements are present. For the two alloys examined, the measurements of the γ' lattice parameter show that

the γ' phase of the ME3 alloy is slightly larger in size as compared to the γ' phase in Rene'88DT, which is likely attributed to the increase in refractory elements.

V. CONCLUSIONS

The γ-γ' lattice parameter changes with temperature and γ-γ' misfit evolution during continuous cooling were characterized for two PM superalloy compositions. For one of the compositions, ME3, results from the continuous cooling study were compared to isothermal experiments to form an understanding of how the time at temperature may influence the lattice parameter evolution. The following general conclusions were obtained from this work:

- For the case of the secondary γ' burst events, evidence of the γ' transformation bursts may be observed from the time-resolved on-cooling diffraction data and is consistent with independently validated differential thermal data.
- From the continuous cooling experiments, the temperature range over which the γ-γ' misfit transitions from negative misfit to positive misfit shows a strong influence from alloy composition for the two alloys characterized.
- Distortions to the fundamental peak intensities were observed at temperatures below the initial γ' burst for both alloys that may suggest evidence of the tertiary γ' precipitation event.
- The transient conditions over the range explored in the current study suggest that starting composition is more influential in the observed, bulk misfit than what may be optimized by processing where the strongest influence on misfit can be attributed to the temperature.

In summary, the characterization performed within this work sheds valuable insight into the real-time evolution of the γ and γ' precipitation events that occur during transient processing of these superalloys following supersolvus solutioning.

REFERENCES

1. R.J. Mitchell, M.C Hardy, M. Preuss, S. Tin: *Superalloys 2004, Proc. Int. Symp., 10th*, pp. 361–70.
2. A.R.P. Singh, S. Nag, S. Chattopadhyay, Y. Ren, J. Tiley, G.B. Viswanathan, H.L. Fraser, and R. Banerjee: *Acta Mater.*, 2013, vol. 61 (1), pp. 280–93.
3. M. Li, J. Coakley, D. Isheim, G. Tian, and B. Shallock: *J. Alloys Compd.*, 2018, vol. 732, pp. 765–76.
4. D.M. Collins, L. Yan, E.A. Marquis, L.D. Connor, J.J. Ciardiello, A.D. Evans, and H.J. Stone: *Acta Mater.*, 2013, vol. 61 (20), pp. 7791–7804.
5. X. Fan, A. Zhang, Z. Guo, X. Wang, J. Yang, and J. Zou: *JOM*, 2019, vol. 54 (3), pp. 2680–89.
6. F. Masoumi, D. Shahriari, M. Jahazi, J. Cormier, and A. Devaux: *Sci. Rep.*, 2016, vol. 6 (1), pp. 1–16.
7. C. Papadaki, W. Li, and A.M. Korsunsky: *Materials*, 2018, vol. 11 (9), p. 1528.
8. P.S. Mathur and J.L. Bartos: *USAAMRDL-TR-76-30*, General Electric Company, Lynn, 1977.
9. S.T. Wlodek, M. Kelly, D.A. Alden: *Superalloys 1996, Proc. Int. Symp., 8th*, pp. 129–36.
10. T.P. Gabb, A. Garg, D.L. Ellis, and K. O'Conner: NASA Report, TM-2004-213066, 2004.
11. S.L. Semiatin, F. Zhang, R. Larsen, L.A. Chapman, and D.U. Furrer: *Integr. Mater. Manuf. Innov.*, 2016, vol. 5 (1), pp. 41–60.
12. J. Gayda, T.P. Gabb, P.T. Kantzos, D.U. Furrer: NASA Report, TM-2002-211558, 2002.
13. R.R. Unocic, L. Kovarik, C. Shen, P.M. Sarosi, Y. Wang, J. Li, M.J. Mills: *Superalloys 2008, Proc. Int. Symp., 11th*, pp. 377-385.
14. A.J. Goodfellow, L.R. Owen, K.A. Christofidou, J. Kelleher, M.C. Hardy, and H.J. Stone: *Metals*, 2019, vol. 9 (6), p. 700.
15. M.V. Nathal, R.A. Mackay, and R.G. Garlick: *Mater. Sci. Eng.*, 1985, vol. 75 (1–2), pp. 195–205.
16. T.M. Pollock and S. Tin: *J. Propul. Power*, 2006, vol. 22 (2), pp. 361–74.
17. J.S. Van Sluytman and T.M. Pollock: *Acta Mater.*, 2012, vol. 60 (4), pp. 1771–83.
18. A. Wisniewski and J. Beddoes: *Mater. Sci. Eng. A*, 2009, vol. 510, pp. 266–72.
19. S.L. Semiatin, S.L. Kim, F. Zhang, and J.S. Tiley: *Metall. Trans. A*, 2015, vol. 46 (4), pp. 1715–30.
20. J. Mao, K. Chang, W. Yang, K. Ray, S. Vaze, D.U. Furrer: *Metall. Trans. A*, 2001, pp. 2441–52.
21. T.P. Gabb, D.G. Backman, D.Y. Wei, D.P. Mourer, D. Furrer, A. Garg, D.L. Ellis: *Superalloys 2000, Proc. Int. Symp., 9th*, pp. 405–14.
22. R.A. Ricks, A.J. Porter, and R.C. Ecob: *Acta Metall.*, 1983, vol. 31 (1), pp. 43–53.
23. Y.S. Yoo, D.Y. Yoon, and A.M. Henry: *Met. Mater.*, 1995, vol. 1 (1), pp. 47–61.
24. A.G. Khachaturyan: *Theory of Structural Transformations in Solids*, Courier Corporation, Chelmsford, 2013.
25. H.J. Stone, T.M. Holden, and R.C. Reed: *Acta Mater.*, 1999, vol. 47 (17), pp. 4435–48.
26. R.Y. Zhang, H.L. Qin, Z.N. Bi, J. Li, S. Paul, and T.L. Lee: *Metall. Trans. A*, 2020, vol. 51 (4), pp. 1860–73.
27. D.M. Collins, D.J. Crudden, E. Alabort, T. Connolley, and R.C. Reed: *Acta Mater.*, 2015, vol. 94, pp. 244–56.
28. M.C. Hardy, M. Detrois, E.T. McDevitt, C. Argyrakis, V. Saraf, P.D. Jablonski, and S. Tin: *Metall. Trans. A*, 2020, vol. 51 (6), pp. 2626–50.
29. D.P. Mourer, K.R. Bain, P.L. Reynolds, J.J. Shirra, and T.P. Gabb: European Patent Application EP1 195 446 A1, 2000.
30. T.P. Gabb, J. Gayda, D.F. Johnson, R.A. MacKay, R.B. Rogers, C.K. Sudbrack, A. Garg, I.E. Locci, S.L. Semiatin: NASA Report, 2016-218936, 2016.
31. J. Cormier: *Superalloys 2016, Proc. Int. Symp., 13th*, pp. 383–94.
32. A.P. Hammersley: ESRF Internal Report, ESRF97HA02T, 1997.
33. A.P. Hammersley, S.O. Svensson, M. Hanfland, A.N. Fitch, and D. Häusermann: *High Press. Res.*, 1996, vol. 14, pp. 235–48.

34. B.E. Warren: *X-Ray Diffraction*, Addison-Wesley, Boston, 1969.
35. B.D. Cullity and S.R. Stock: *Elements of X-ray Diffraction*, 3rd ed., Prentice Hall, New Jersey, 2001, pp. 348–55.
36. J.O. Andersson, T. Helander, L. Höglund, P.F. Shi, and B. Sundman: *Calphad*, 2002, vol. 26, pp. 273–312.
37. T.P. Gabb, A. Garg, D.L. Ellis: NASA Report, TM-2004-213123, 2004.
38. G. Esteves, K. Ramos, C.M. Fancher, J.L. Jones: LIPRAS: Line-Profile Analysis Software, 2017. https://doi.org/10.13140/rg.2.2.29970.25282/3.
39. D.A. Porter, K.E. Easterling, M.Y. Sherif: *Phase Transformations in Metals and Alloys*. 3rd ed., Taylor & Francis Group LLC, 2009.
40. C. Shen, Modeling Creep-Fatigue-Environment Interactions in Steam Turbine Rotor Materials for Advanced Ultra-supercritical Coal Power Plants (2014). https://www.osti.gov/servlets/purl/1134364.
41. T.P. Gabb, J. Gayda, J. Telesman, P.T. Kantzos: NASA Report, 20050186902, 2005.
42. S. Huang, K. An, Y. Gao, and A. Suzuki: *Metall. Mater. Trans. A*, 2018, vol. 49 (3), pp. 740–51.
43. G.B. McBride: *Using Statistical Methods for Water Quality Management*, Wiley, New York, 2005, pp. 305–13.
44. J. Mao, K.M. Chang, W. Yang, D.U. Furrer, K. Ray, and V.P. Vaze: *Mater. Sci. Eng. A*, 2002, vol. 332 (1–2), pp. 318–29.
45. D.M. Collins, N. D'Souza, C. Panwisawas, C. Papadaki, G.D. West, and P. Kontis: *Acta Mater.*, 2020, vol. 200, pp. 959–70.
46. S.L. Semiatin, N.C. Levkulich, and J.S. Tiley: *Metall. Trans. A*, 2019, vol. 50 (11), pp. 5281–96.
47. J. Tiley, R. Srinivasan, R. Banerjee, G.B. Viswanathan, B. Toby, and H.L. Fraser: *Mater. Sci. Technol.*, 2009, vol. 25 (11), pp. 1369–74.
48. S.L. Semiatin, D.W. Mahaffey, N.C. Levkulich, O.N. Senkov, and J.S. Tiley: *Metall. Trans. A*, 2018, vol. 49 (12), pp. 6265–76.
49. Y.U. Wang, Y.M. Jin, and A.G. Khachaturyan: *J. Appl. Phys.*, 2002, vol. 92 (3), pp. 1351–60.
50. M. Akhlaghi, T. Steiner, S.R. Meka, and E.J. Mittemeijer: *J. Appl. Crystallogr.*, 2016, vol. 49 (1), p. 69.